Nanoscale

PAPER

View Article Online
View Journal | View Issue

Cite this: *Nanoscale*, 2025, **17**, 6854

Contactless health monitoring in autonomous self-reporting ceramic coatings†

Peter J. Pöllmann, *‡[a] Sebastian Lellig, *‡[a,b] Dimitri Bogdanovski, [a] Amir Hossein Navidi Kashani, [a] Damian M. Holzapfel, [a] Clio Azina, [a] Peter Schweizer,[b] Marcus Hans, [a] Paula Zöll,[a] Daniel Primetzhofer, [c] Szilárd Kolozsvári,[d] Peter Polcik,[d] Johann Michler[b,e] and Jochen M. Schneider [a,f]

Autonomous tracking of structural changes in coated components yields information on materials health and remaining lifetime; but until now, electrical resistance tracking required undesired physical connections between coating and readout. Here, the proof of concept for contactless tracking of phase transformations in autonomous self-reporting Cr–Al–B coatings is demonstrated. Contactless monitored electrical resistance changes of glassy $Cr_{0.34}Al_{0.31}B_{0.35}$ coatings reveal crystallization, phase formation, and grain growth of Cr_3AlB_4 and Cr_2AlB_2. The hitherto untapped potential of contactless measured electrical resistance data for assessing materials health by tracking structural change is revealed by *in situ* high-resolution scanning transmission electron microscopy and selected area electron diffraction as well as *ex situ* X-ray diffraction, and elastic-recoil detection analysis. Continuous or periodic contactless tracking of material health data will enable more efficient and more sustainable materials service by utilizing the individual remaining component lifetime rather than the much shorter lifetime assessment emanating from safety factor-based design approaches.

Received 17th September 2024,
Accepted 13th February 2025

DOI: 10.1039/d4nr03822c

rsc.li/nanoscale

Introduction

Extending the service life of components aligns materials design efforts with the United Nations Sustainable Development Goal 12, titled "responsible consumption and production".[1] Often, materials lifetime assessments are based on statistical data in combination with safety factors.[2,3] Depending on the width of the statistical distribution and the magnitude of the safety factor, components are taken out of service long before their actual end of life. Clearly, tracking health data of coating materials during application would enable a more sustainable material consumption as the individual component lifetime is significantly increased. Thus, employing self-reporting materials, where the unmodified material acts as a sensor, possessing a material property that has a causal relationship with structural and/or chemical changes,[4] might yield significant benefits for reaching the UN's goal.

Steps in this direction have been taken by tracking changes in color,[5–8] photoluminescence,[7,9–13] or electrical resistance[14–18] as response to mechanical loading, resulting in strain generation in polymers,[5,9,10] composites,[7,13] liquid crystals,[8] and ceramics,[11] crack formation in polymers[6,7] as well as composites,[14–18] and scratches in metals.[12]

Also, polymers containing a second sensing phase have been designed to report electrical degradation by color changes.[19] Chemical changes have been tracked by observing color,[20–22] photoluminescence,[23] or electrical resistance[4] variations in dual-phase polymers,[20] polymer-metal composites,[21–23] and in ceramic materials.[4]

A phase separation due to heat exposure has been reported by changes in the fluorescence of polymer blends.[24] Moreover, phase changes from amorphous to a crystalline disordered solid and a subsequent phase transition to an ordered structure have been tracked by contact-based electrical resistance measurements during vacuum annealing of Cr_2AlC protective coatings.[25] It was shown that phase transitions could be related to distinct modulations of the temperature-dependent, *in situ* measured electrical resistance. Hence, Cr_2AlC serves as protective coating and at the same time as sensor for phase transitions.

From the literature review above, it is evident that self-reporting materials can convey information pertaining to

[a]*Materials Chemistry, RWTH Aachen University, Aachen, Germany. E-mail: poellmann@mch.rwth-aachen.de, lellig@mch.rwth-aachen.de*
[b]*Empa, Swiss Federal Laboratories for Materials Science and Technology, Laboratory for Mechanics of Materials and Nanostructures, Thun, Switzerland*
[c]*Department of Physics and Astronomy, Uppsala University, Uppsala, Sweden*
[d]*Plansee Composite Materials GmbH, Lechbruck am See, Germany*
[e]*École Polytechnique Fédérale de Lausanne (EPFL), 1015 Lausanne, Switzerland*
[f]*Max-Planck-Institute for sustainable materials GmbH, Department Structure and Nano-/Micromechanics of Materials, Group Self-Reporting Materials, Düsseldorf, Germany*

†Electronic supplementary information (ESI) available. See DOI: https://doi.org/10.1039/d4nr03822c

‡These authors contributed equally to the publication.

mechanical loading, structural changes as well as electrical and chemical degradation.

Recently, proof of concept for tracking materials health data at temperatures >500 °C in harsh environments has been demonstrated *via* resistivity measurements utilizing physical contacts attached to the monitored material surface.[25] This methodology is, however, extremely challenging to be utilized in real life applications with fast-moving components operating in harsh environments. We therefore propose a simple contactless method for gauging the materials health status of $Cr_{0.34}Al_{0.31}B_{0.35}$ coatings (Fig. 1), without the need for a secondary sensor phase, revealing phase transitions due to high-temperature exposure by modulations in electrical resistance. We verify contactless-obtained data by comparison to well-established contact-based resistance measurements as well as *in situ* and *ex situ* structural and chemical analyses. Hence, we demonstrate the proof of concept for contactless tracking of materials health-relevant data, namely multiple phase transitions occurring between room temperature and 800 °C.

Principle of contactless phase transition detection

Annealing of amorphous $Cr_{0.34}Al_{0.31}B_{0.35}$ coatings (Fig. 1a) triggers two amorphous to crystalline phase transitions: between 400 and 500 °C, the formation of the Cr_2AlB_2 MAB phase, a member of the nanolaminated transition metal borides, whereby M corresponds to an early transition metal, A for an A-group element and B for Boron, is inferred, see Fig. 1b and ESI S7–9,† and between 500–600 °C, the formation of the

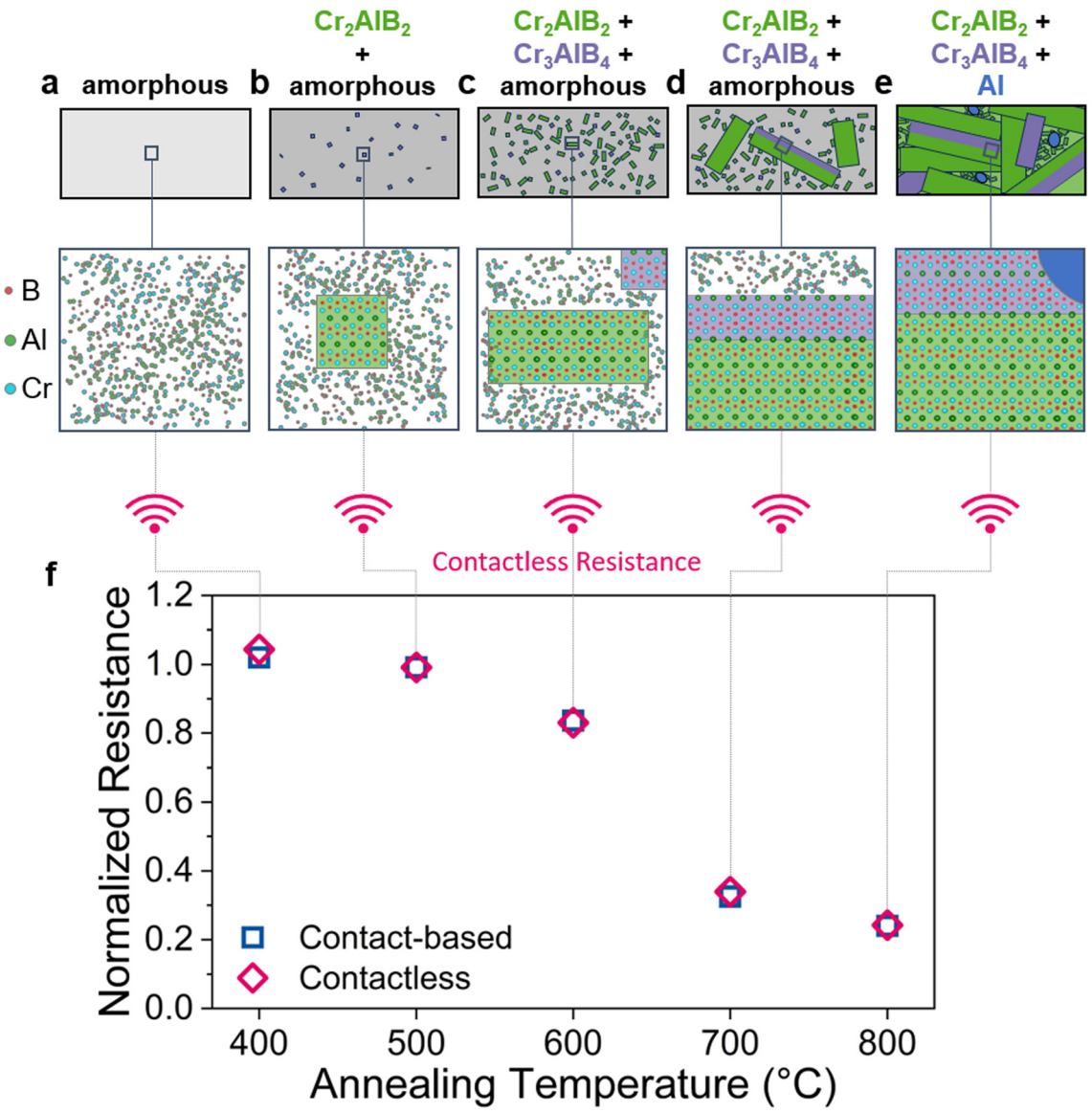

Fig. 1 Schematic illustration of crystal structure and grain size after annealing (a–e). Contact-based and contactless measured, normalized resistance *versus* annealing temperature (f) showing a crystal structure and grain size dependent resistivity decrease with increasing annealing temperature. Resistance data are normalized with respect to their initial value before annealing.

Cr_3AlB_4 MAB phase is detected, see Fig. 1c. These observations are consistent with contact-based and contactless normalized resistance measurements, calorimetry, and spatially resolved structure analysis, which are in very good agreement. Accelerated growth of Cr_2AlB_2 and Cr_3AlB_4 from the amorphous precursor phase is observed between 600 and 700 °C (Fig. 1d). Between 700 and 800 °C, the complete transformation of the amorphous phase into crystalline Cr_2AlB_2 and Cr_3AlB_4 MAB phases as well as into liquid Al is inferred, see Fig. 1e. Hence, we show proof of concept for remote tracking of complex combinations between phase transitions and grain growth by contact-based resistance measurements as well as by contactless resistance measurements, which are in excellent agreement with the former (Fig. 1f). We envision that contactless tracking of materials health data in harsh environments and on complex-shaped components will extend the service life thereof and hence enable more sustainable materials consumption.

Referencing with contact-based resistance and calorimetry

To demonstrate the proof of concept for contactless tracking of temperature-dependent materials health data, calorimetric data, indicating three phase transitions, is compared to the normalized *ex situ* measured contactless resistance and the normalized *in situ* measured contact-based resistance, see Fig. 2g. The maximum deviation between contact-based and contactless measured resistance data is 4% and hence, they exhibit very good agreement (Fig. 1f and ESI S1†). Therefore, we refer to both, contactless and contact-based measured resistance values simply as resistance. Resistance measurements between room temperature and 400 °C reveal a negative thermal coefficient of resistance (TCR), characteristic for glassy structures.[26,27] Subsequently, at ~450 °C, the temperature dependent resistance signal exhibits a pronounced change in slope, as revealed by the non-linear behavior of the first derivative of the measured resistance with temperature (dR/dT *vs.* T). Over the whole, here investigated temperature range, three well defined peaks in dR/dT *vs.* T can be seen. Interestingly, the onset and peak temperatures in dR/dT *vs.* T show, with maximum deviations of 7 and 18 °C, excellent agreement with the corresponding temperatures as obtained from calorimetry, see Fig. 2g. The significance of this observation for tracking materials health data with resistivity measurements is highlighted by the corresponding structural analysis data from high-resolution scanning transmission electron microscopy (HRSTEM, *ex situ* Fig. 2a–f, *in situ* Fig. 4), selected area electron diffraction (SAED, Fig. 3 and ESI S3†) and X-ray diffraction (XRD, ESI S4†). The average chemical composition of the films was not significantly altered by the annealing as is evident from elastic recoil detection analysis (ERDA, ESI S2†). The slight offset measured between the calorimetric data and the temperature-dependent resistance data can be rationalized by differences in sample nature and experimental protocol: for the resistance measurement a thin film on a substrate was heated in vacuum, while the calorimetry measurements were conducted on powder samples in an Argon atmosphere.

While up to 400 °C, no evidence for phase transformations can be inferred from HRSTEM and *in situ* SAED measurements (Fig. 3b, d and ESI S3†), the onset of a first transformation is identified by a change in the *in situ* SAED peak shape at 450 °C between 1.5 and 3 Å, see Fig. 3d and ESI S5.† A decrease in diffracted intensity at $d < 2.25$ Å in combination with an intensity increase at $d > 2.25$ Å, signaling a shift towards peak positions indicating formation of crystalline phases. This interpretation is consistent with the temperature dependent crystallization depicted in the diffractograms shown in ESI S3.† Moreover, evidence for nucleation of a crystalline phase can be seen in the HRSTEM image of the sample annealed to 500 °C, see Fig. 2b. A more detailed analysis of phase formation, based on XRD and SAED, given in the ESI infers the formation of Cr_2AlB_2 at these temperatures (ESI S6–8†). These characteristic manifestations of an amorphous – crystalline phase transition coincide with both, the onset of the first peak identified in the dR/dT signal as well as the onset of the first enthalpic peak in the calorimetric data, see orange colored region in Fig. 2g at 451 and 458 °C, respectively. Hence, changes in dR/dT *vs.* T indicate the onset of phase transitions. Moreover, as the peak position of dR/dT *vs.* T at 518 °C aligns with the first peak of the DSC signal at 515 °C, it is evident that dR/dT *vs.* T tracks the amorphous to crystalline phase transition in $Cr_{0.34}Al_{0.31}B_{0.35}$ coatings.

A second transformation is indicated by the blue colored region in Fig. 2g displaying calorimetric data with onset and peak temperatures of 548 °C and 572 °C, respectively. The HRSTEM micrograph in Fig. 2c shows a crystallite containing Cr_3AlB_4 and Cr_2AlB_2 domains, consistent with the *in situ* SAED data displayed in Fig. 3d at 600 °C. These observations also concur with *in situ* HRSTEM data, as displayed in Fig. 4d, as well as with *ex situ* XRD data as shown in ESI S4.† The formation of Cr_3AlB_4 at these temperatures is further inferred from the more detailed phase formation analysis given in ESI S6–8. The above discussed onset and peak temperatures obtained by calorimetry, indicating the 2nd transition, coincide with the onset and peak temperatures in dR/dT *vs.* T at 551 °C and 590 °C, respectively. Hence, dR/dT *vs.* T was demonstrated to track both phase transformations discussed so far.

A third transformation is indicated in the red colored region in Fig. 2g, displaying DSC data with onset and peak temperatures of 660 °C and 696 °C, respectively. From the comparison of *in situ* HRSTEM micrographs, Fig. 4, taken during annealing at 600 °C (Fig. 4d), 700 °C (Fig. 4e), and 750 °C (Fig. 4f), it is evident that the observed peak in DSC data corresponds to accelerated grain growth occurring in this temperature regime, as has been shown before for nanocomposite TiB_xN_y and TiB_xC_y coatings[28,29] as well as nanocrystalline Cu powders.[30] Furthermore, the video recorded at 750 °C (ESI S9†) supports this interpretation, showing atomic scale, layer-by-layer growth of a crystal containing intergrown structures of both Cr_2AlB_2 and Cr_3AlB_4 MAB phases, similar to what has been observed for $(Mo,Cr)_2AlB_2$[31] and MoAlB MAB phases.[32–34] Hence, based on *in situ* HRSTEM investigations, it is inferred that accelerated grain growth is causing the exother-

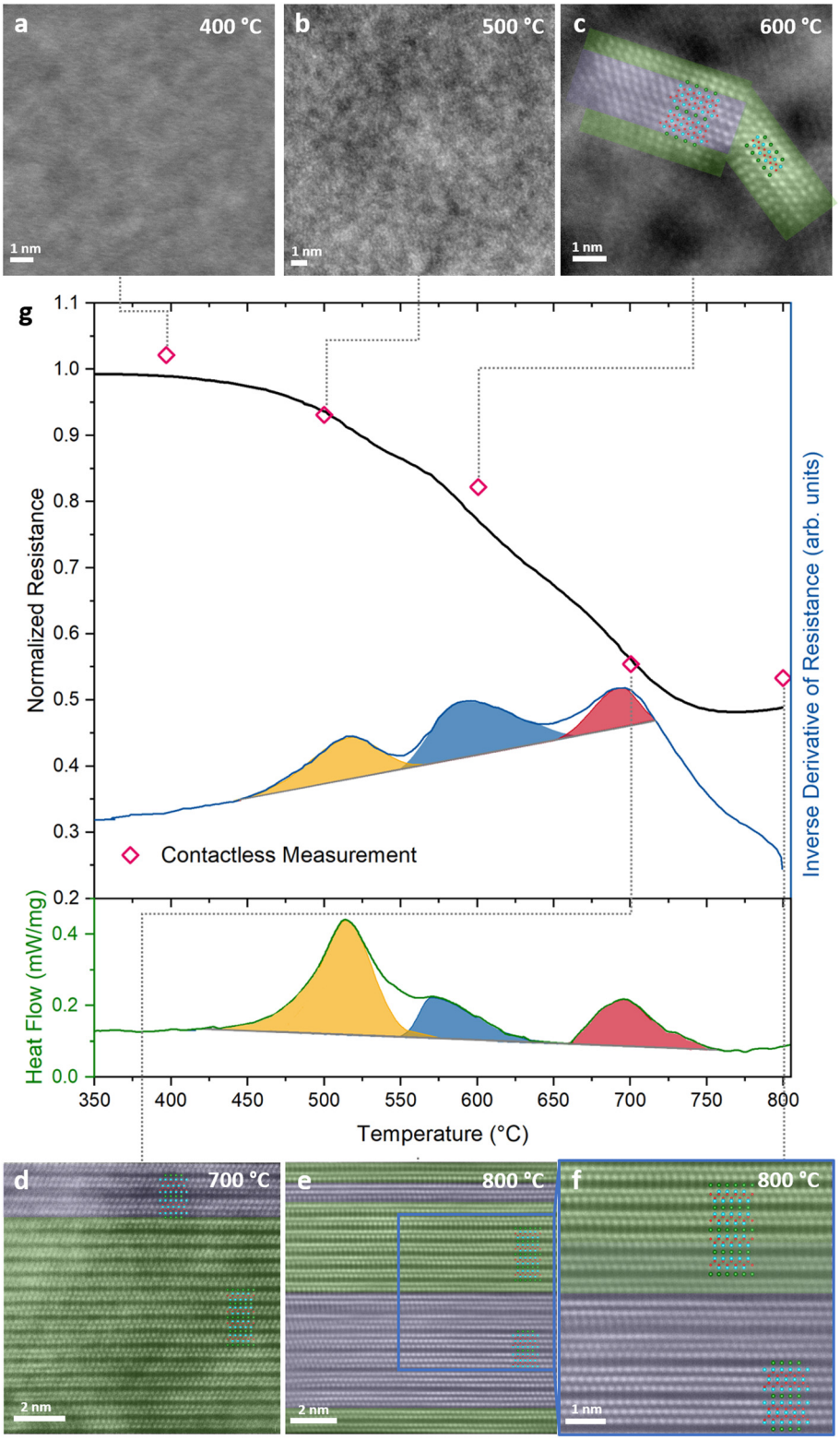

Fig. 2 *Ex situ* HRSTEM images with overlays of ideal structures (blue atoms corresponding to Cr, green atoms to Al, and red atoms to B) and colored areas where Cr_2AlB_2 (green) and Cr_3AlB_4 (purple) are identified (a–e). A higher magnification image of the region marked in blue borders in (e) is shown in (f). In situ contact-based measured resistance normalized with respect to its initial room temperature value (black curve, top) and the derivative d*R*/d*T versus* temperature (blue curve, top) along with contactless measured resistance (magenta diamonds) measured at room temperature and multiplied with the thermal coefficient of resistance determined for the respective sample and calorimetric measurement (green curve, bottom) (g). Peaks in the calorimetric data as well as in d*R*/d*T versus T* were colored as a guide for the eye.

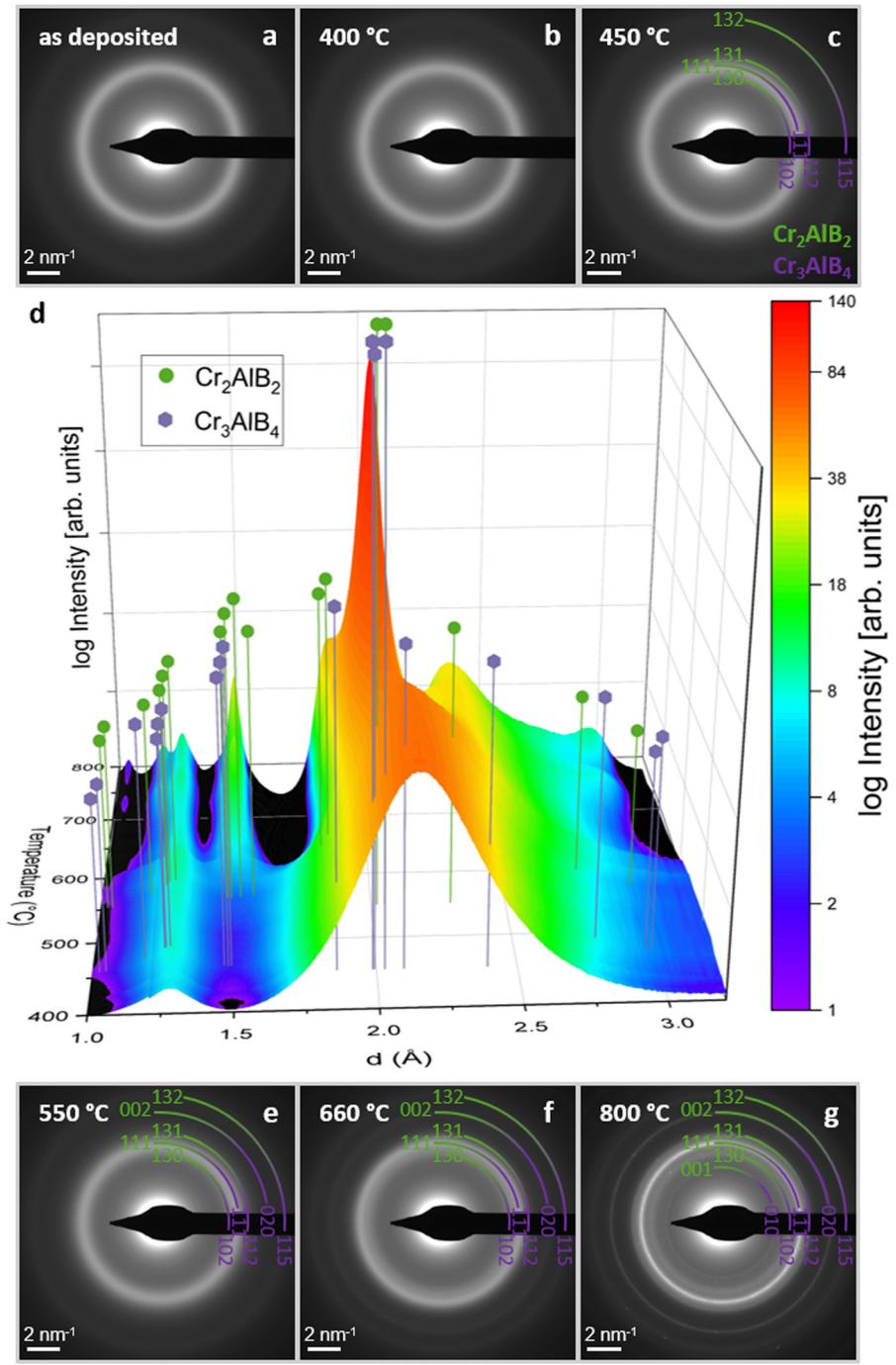

Fig. 3 In situ SAED patterns (a–c and e–g) and the corresponding integrated intensity plotted with respect to temperature (d). Peak positions of Cr_2AlB_2 and Cr_3AlB_4 are indicated. A first transformation is visible at 450 °C (see ESI S5†) with subsequent emergence of peaks corresponding to Cr_2AlB_2 and Cr_3AlB_4.

mal reaction captured in the corresponding calorimetric data set. Further supporting evidence for the above observed accelerated grain growth of both Cr_3AlB_4 and Cr_2AlB_2 is obtained by comparing the HRSTEM micrographs obtained after annealing to 600 °C, see Fig. 2c, to the 700 °C anneal shown in Fig. 2d. Also, the SAED data displayed in Fig. 3d and the XRD data shown in ESI S4† are exhibiting significant peak intensity increases and concomitant decreases in full-width at half maximum for Cr_3AlB_4 and Cr_2AlB_2 diffraction signals and are therefore consistent with the grain coarsening notion. This accelerated reaction can be rationalized based on melting of excess Al, present since the overall chemical composition contains 33 at% Al while the 212 and the 314 phase only contain 20 at% and 12.5 at%, respectively. In Fig. S10,† the DSC

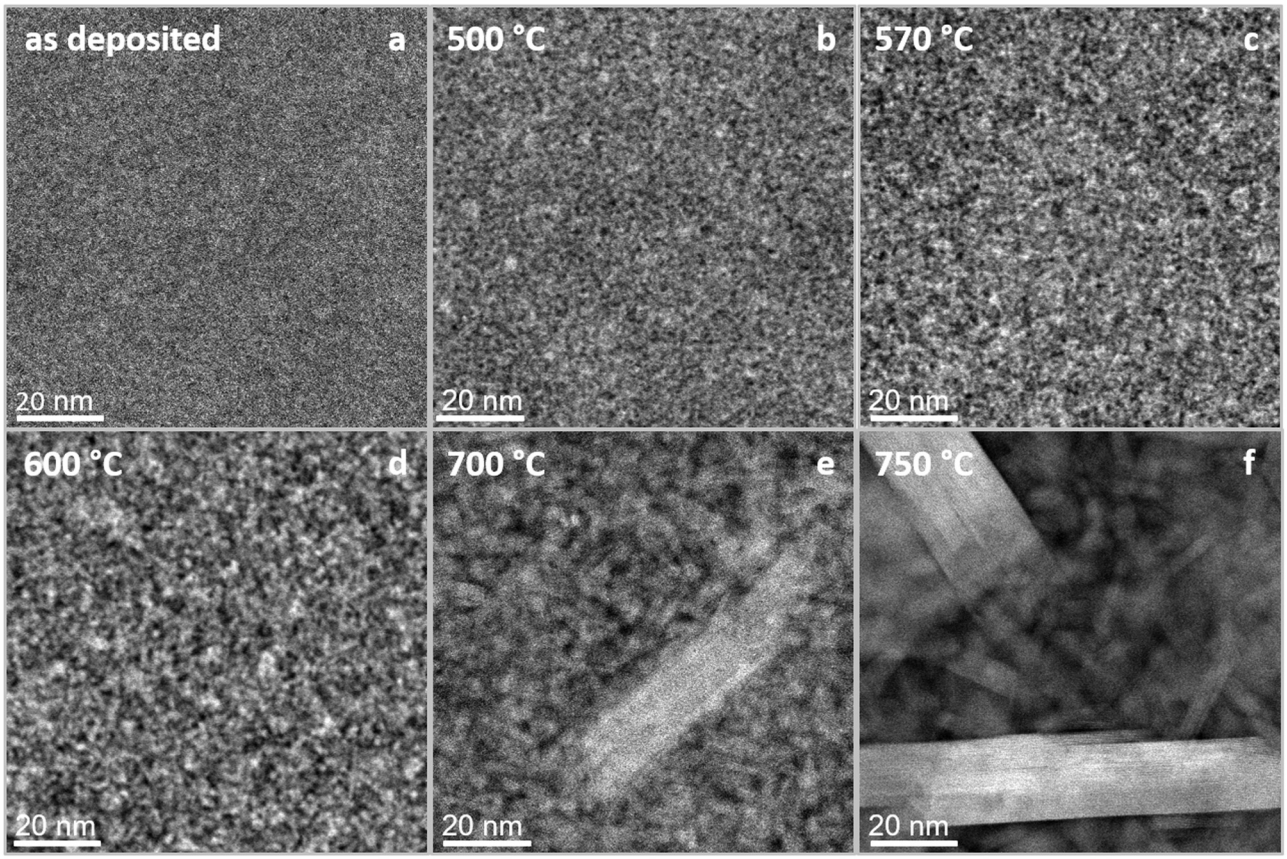

Fig. 4 HRSTEM micrographs taken during *in situ* annealing at indicated temperatures (a–f). The amorphous as deposited structure becomes partly crystalline after 500 °C, whereby MAB phase formation is observed, with a significant increase in crystal domain size after 700 °C.

heating curves for repeated heating cycles of one sample are shown. In the first three heating cycles depicted by the blue (1st cycle), green (2nd cycle) and yellow (3rd cycle), exothermic signals indicate the crystalline amorphous transition as discussed above, consistent with the DSC data presented in Fig. 2. The DSC data of the 4th heating cycle (red curve) indicates that the amorphous to crystalline transition was completed during the first 3 heating cycles as an endothermic peak at ~640 °C, which coincides with the melting point reported for Al (659 °C),[35]is visible. The small endothermic peak is concealed by the exothermic signal associated with the amorphous to crystalline transition tracked in a single heating run as it takes place simultaneously, see Fig. 2. This notion is supported by the peaks corresponding to elemental Al visible in the XRD after cooling (ESI S4†). After the third transformation, the previously decreasing trend of resistance is reversed since grain growth and phase formation have been completed leading to a now positive TCR as expected for MAB phases.[36–38]

As for both above discussed phase transitions, the agreement for the third transition, marked in red in Fig. 2g, between dR/dT *vs.* T and the DSC data sets regarding onset and peak position temperatures is, with a maximum deviation of 5 °C, very good.

Hence, we have demonstrated that three different phase transformations can be tracked by *in situ* contact-based resistance measurements. Furthermore, *ex situ* contactless electrical resistance measurements mirror the trend displayed by the contact-based measurement: The agreement between both methods, displayed in Fig. 1f, is excellent as the differences are ≤4% for the entire here investigated temperature range. Thus, by relating periodic contactless measurements to the preceding structural analysis, the current state of the material can be inferred. Therefore, the proof of concept for contactless materials health tracking has been demonstrated. Other potential candidates for application include, for example, TiAlN thin films, that show different recovery processes, phase transitions and spinodal decomposition as observed by DSC measurements.[39] Especially the technologically-relevant decomposition would be of interest due to the large difference in the electrical resistivities of the binary nitrides TiN and AlN, which is also expressed in a close to exponential increase in the resistivity of TIAlN upon Al addition for an Al content between 7.9 and 51.5 at%.[40] As the electrical resistance of materials is generally affected by changes in the environment, materials health data tracking can be envisioned for a wide range of applications in harsh environments, where physical and/or chemical changes are triggered by mechanical, thermal, or chemical stressors.

While the contact-based measurement required four physical contact wires attached to the sample surface and measurement times of about 30 seconds per data point, the contactless measurement time is around 1 second. Considering that it is a mechanical and electrical engineering exercise to integrate contactless resistance measurement technology into complex shaped coated components, the dynamic assessment of dR/dT *vs.* T at high speeds in harsh environments appears feasible from a fundamental science perspective. We envision that materials health monitoring by contactless electrical resistance measurements enables a more sustainable materials usage as the individual remaining component lifetime is assessed and can replace component operation relying on safety factor-based design.

Conclusions

In summary, amorphous $Cr_{0.34}Al_{0.31}B_{0.35}$ coatings were annealed in vacuum and three phase transformations were identified. It was shown that these phase changes can be tracked with *in situ* contact-based as well as *ex situ* contactless resistance data *via* comparison to XRD, DSC, ERDA as well as *ex situ* and *in situ* HRSTEM and SAED data measured in the corresponding temperature ranges. The contactless resistance data are, with deviations ≤4%, in excellent agreement with contact-based resistance data. Therefore, it is demonstrated that contactless resistance data are useful for assessing materials health by tracking structural changes in $Cr_{0.34}Al_{0.31}B_{0.35}$ coatings. Contactless resistance tracking can in principle be integrated into coated components operating at high speeds in harsh environments and is thereby expected to enable a more sustainable usage, as the individual remaining component lifetime is tracked, replacing component operation based on designs utilizing safety factors.

Methods

Synthesis of Cr–Al–B thin films

Amorphous Cr–Al–B thin films were synthesized by direct current magnetron sputtering (DCMS) without intentional heating in a high vacuum deposition system with a base pressure below 9×10^{-7} mbar. A 2″ ternary 1 : 1 : 1 Cr : Al : B target (Plansee Composite Materials GmbH, Lechbruck am See, Germany) was run at a constant power of 120 W facing the floating single crystalline 10 × 10 cm Al_2O_3 (0001) substrate at a distance of 10 cm. An argon pressure of 0.3 Pa and a deposition time of 60 min led to films with a thickness of ∼0.8 μm.

Electrical resistance measurements

Contact-based electrical resistance was measured using the Van-der-Pauw method.[41,42] The *in situ* measurement setup utilized here was identical to previous experiments and is described in more detail elsewhere.[4,25] The heating and cooling rate was kept constant at 10 K min^{-1} while the pressure in the vacuum furnace was below 5×10^{-6} mbar. To determine significant changes in R *vs.* T, the first derivative of the resistance was computed with respect to T (dR/dT). The onset and peak temperatures of dR/dT *vs.* T were fitted by using a bi-Gaussian function.[43] The thermal coefficient of resistance (TCR) was extracted from the linear slope of the cooling curves.

Contactless resistance was determined using Eddy-current measurements carried out *ex situ* for samples annealed to the indicated temperatures in an EddyCus TF lab 2020SR (SURAGUS GmbH, Dresden, Germany) performing self-referencing before every measurement session. For each sample, two measurements were averaged to obtain the sheet resistance R_S, which was then used to calculate the resistivity (ρ) by multiplying it with the film thickness (d) according to $\rho = R_S \cdot d$. The highest determined variation for repeated measurements of one sample was <0.6%.

X-ray diffraction

Phase formation was studied by Bragg–Brentano X-ray diffraction (XRD) in a Panalytical Empyrean MRD diffractometer (Malvern Panalytical, Almelo, The Netherlands) equipped with a Cu Kα source and operated at a current of 40 mA and a voltage of 40 kV. Scans were recorded with a – 5° omega offset scan with a step size of 0.026° and a measurement time of 100 s per step. Powder diffraction files (PDF) of Cr_2AlB_2 (01-084-8899), Cr_3AlB_4 (01-084-8900), and Al (04-0787) were used for phase identification.

Crystallization kinetics

Crystallization kinetics were studied by differential scanning calorimetry (DSC) in a Jupiter® STA 449 C (Netzsch GmbH, Selb, Germany) with a continuous heating mode (heating rate 10 K min^{-1}) in Ar atmosphere (purity 99.9999%). Low oxygen content (<1 ppm) in the atmosphere was ensured by the integrated oxygen trap system (OTS®). Temperature and sensitivity were calibrated by melting high purity standards (≥99.9%) (Zn, Sn, Al, Ag, Au, Pd) and the onset temperatures of the reactions were extracted using the tangent method.[44] As a guide for the eye, the exothermal peaks were schematically colored in the graphical representation. The powder for the experiments was generated by deposition of a film on a NaCl substrate and subsequent dissolution thereof.[45]

Compositional analysis

The chemical composition depth profile of the films was quantified by time-of-flight elastic recoil detection analysis (ToF-ERDA) at the Tandem Accelerator Laboratory of Uppsala University[46] using a 36 MeV $^{127}I^{8+}$ primary beam. The angle between the primary beam and the detector telescope was 45°, while the incidence and exit angles of the primary ions and detected recoils with respect to the film surface were 22.5°. Energy discrimination was done by using a gas detector system[47] and the time-of-flight was determined with thin carbon foils.[48] Depth profiles were obtained from time-energy coincidence spectra using CONTES.[49] The films were found to

be homogeneous and average concentrations were calculated from the depth profiles, while the oxygen-rich surface-near region was excluded. For B, a maximum total uncertainty of 5% of the determined values is assumed, and aliquot fractions thereof for the metals Cr and Al.

High-resolution analysis

Thin lamellae (<100 nm) for high-resolution scanning transmission electron microscopy (HRSTEM) investigations were prepared by focused ion beam (FIB) techniques in a Helios 5 Hydra UX dual-beam microscope (Thermo Fisher Scientific, Waltham, USA). Xe^+ ions were employed at 30 kV for the standard lift-out procedure onto an omniprobe lift-out grid. Thinning of the lamellae was carried out with Ga^+ ions in a Helios Nanolab 600 dual-beam system (Thermo Fisher Scientific, Waltham, USA). These lamellae were subsequently analyzed in a Titan Themis 200 G3 equipped with a SuperX EDX detector (Thermo Fisher Scientific, Waltham, USA) at an acceleration voltage of 200 kV.

For *in situ* HRSTEM as well as selected area electron diffraction (SAED) heating experiments, Wildfire nano-chips (DENS Solutions, Delft, The Netherlands) were coated with <50 nm of the Cr–Al–B in equivalent conditions to all other films. For the SAED experiments, a constant heating rate of 10 K min^{-1} was applied, while for the HRSTEM imaging, the annealing was interrupted by quenching at specific temperatures to further investigate critical events. The integrated SAED patterns were post-processed for the 3-dimensional graph by partly subtracting an as deposited spectrum as well as the background to showcase the changes induced by annealing. Furthermore, the spectra were corrected for the thermal expansion during the measurement. For phase identification, PDF of Cr_2AlB_2 (01-084-8899) and Cr_3AlB_4 (01-084-8900) were used.

Author contributions

P.J.P.: conceptualization, methodology, formal analysis, investigation (lead), data curation, writing – original draft, and visualization. S.L.: conceptualization, methodology, formal analysis, investigation (lead), data curation, writing – original draft, and visualization. D.B.: investigation, and writing – review, and editing. A.H.N.K.: investigation, formal analysis, and writing – review and editing. D.M.H.: investigation, formal analysis, and writing – review and editing. C.A.: investigation, formal analysis, data curation, and writing – review and editing. P.S.: investigation, formal analysis, and writing – review and editing. M.H.: investigation, formal analysis, data curation, and writing – review and editing. P.Z.: investigation and writing – review and editing. D.P.: investigation, formal analysis, writing – review and editing, and funding acquisition. S. K.: resources and writing – review and editing. P.P.: resources and writing – review and editing. J.M.: conceptualization, methodology, funding acquisition, supervision, and writing – review and editing. J.M.S.: conceptualization, methodology, project administration, writing – original draft, supervision, and funding acquisition.

Data availability

The data supporting this article have been included as part of the ESI.†

Conflicts of interest

The authors declare no competing interests.

Acknowledgements

J. M. S. acknowledges financial support from the MPG fellow program. Transnational access to ion beam analysis has been supported by the RADIATE project under Grant Agreement 824096 from the EU Research and Innovation programme HORIZON 2020. Accelerator operation at Uppsala University has been supported by the Swedish research council VR-RFI under grant agreement 2019-00191.

References

1 United-Nations, *The Sustainable Development Goals Report 2023: Special Edition*, 2023.
2 F. M. Burdekin, *Eng. Failure Anal.*, 2007, **14**, 420–433.
3 E. Roos, G. Wackenhut, R. Lammert and X. Schuler, *Int. J. Pressure Vessels Piping*, 2011, **88**, 19–25.
4 B. Stelzer, M. Momma and J. M. Schneider, *Adv. Funct. Mater.*, 2020, 2000146, DOI: 10.1002/adfm.202000146.
5 D. A. Davis, A. Hamilton, J. Yang, L. D. Cremar, D. Van Gough, S. L. Potisek, M. T. Ong, P. V. Braun, T. J. Martínez, S. R. White, J. S. Moore and N. R. Sottos, *Nature*, 2009, **459**, 68–72.
6 J. Xiao, L. Jia, K. Zhang and X. Wang, *Adv. Eng. Mater.*, 2023, **25**, 2300331.
7 O. Rifaie-Graham, E. A. Apebende, L. K. Bast and N. Bruns, *Adv. Mater.*, 2018, **30**, 1705483.
8 Y.-K. Kim, X. Wang, P. Mondkar, E. Bukusoglu and N. L. Abbott, *Nature*, 2018, **557**, 539–544.
9 N. Bruns, K. Pustelny, L. M. Bergeron, T. A. Whitehead and D. S. Clark, *Angew. Chem., Int. Ed.*, 2009, **48**, 5666–5669.
10 Q. Wang, G. R. Gossweiler, S. L. Craig and X. Zhao, *Nat. Commun.*, 2014, **5**, 4899.
11 V. K. Tolpygo, D. R. Clarke and K. S. Murphy, *Surf. Coat. Technol.*, 2004, **188–189**, 62–70.
12 L. Fang, A. Yin, S. Zhu, J. Ding, L. Chen, D. Zhang, Z. Pu and T. Liu, *J. Alloys Compd.*, 2017, **727**, 735–743.
13 K. Makyła, C. Müller, S. Lörcher, T. Winkler, M. G. Nussbaumer, M. Eder and N. Bruns, *Adv. Mater.*, 2013, **25**, 2701–2706.
14 J. Zhang, J. Liu, R. Zhuang, E. Mäder, G. Heinrich and S. Gao, *Adv. Mater.*, 2011, **23**, 3392–3397.

15 L. Gao, E. T. Thostenson, Z. Zhang and T.-W. Chou, *Adv. Funct. Mater.*, 2009, **19**, 123–130.
16 S.-L. Gao, R.-C. Zhuang, J. Zhang, J.-W. Liu and E. Mäder, *Adv. Funct. Mater.*, 2010, **20**, 1885–1893.
17 E. J. Markvicka, R. Tutika, M. D. Bartlett and C. Majidi, *Adv. Funct. Mater.*, 2019, **29**, 1900160.
18 O. T. Picot, V. G. Rocha, C. Ferraro, N. Ni, E. D'Elia, S. Meille, J. Chevalier, T. Saunders, T. Peijs, M. J. Reece and E. Saiz, *Nat. Commun.*, 2017, **8**, 14425.
19 X. Huang, S. Zhang, P. Zhang, Y. Zhu, J. Xie, M. Yang, L. Han, J. Hu, Q. Li and J. He, *Nat. Mater.*, 2024, **23**, 237–243.
20 X. Hu, G. Li, J. Huang, D. Zhang and Y. Qiu, *Adv. Mater.*, 2007, **19**, 4327–4332.
21 J.-P. Wang, X. Song, J.-K. Wang, X. Cui, Q. Zhou, T. Qi and G. L. Li, *Adv. Mater. Interfaces*, 2019, **6**, 1900055.
22 C. Liu, H. Wu, Y. Qiang, H. Zhao and L. Wang, *Corros. Sci.*, 2021, **184**, 109355.
23 J.-P. Wang, J.-K. Wang, Q. Zhou, Z. Li, Y. Han, Y. Song, S. Yang, X. Song, T. Qi, H. Möhwald, D. Shchukin and G. L. Li, *Macromol. Mater. Eng.*, 2018, **303**, 1700616.
24 B. R. Crenshaw and C. Weder, *Adv. Mater.*, 2005, **17**, 1471–1476.
25 B. Stelzer, X. Chen, P. Bliem, M. Hans, B. Volker, R. Sahu, C. Scheu, D. Primetzhofer and J. M. Schneider, *Sci. Rep.*, 2019, **9**, 7.
26 J. H. Mooij, *Phys. Status Solidi A*, 1973, **17**, 521–530.
27 U. Mizutani, *Phys. Status Solidi B*, 1993, **176**, 9–30.
28 P. H. Mayrhofer and C. Mitterer, *Surf. Coat. Technol.*, 2000, **133–134**, 131–137.
29 P. H. Mayrhofer, H. Willmann and C. Mitterer, *Thin Solid Films*, 2003, **440**, 174–179.
30 J. Liu, H. Cui, X. Zhou and J. Zhang, *Mater. Trans.*, 2012, **53**, 766–769.
31 P. J. Pöllmann, D. Bogdanovski, S. Lellig, P. Schweizer, M. Hans, C. Azina, S. Karimi Aghda, P. Zöll, D. M. Holzapfel, D. Primetzhofer, S. Kolozsvári, P. Polcik, J. Michler and J. M. Schneider, *Mater. Res. Lett.*, 2024, **12**, 58–66.
32 R. Sahu, D. Bogdanovski, J.-O. Achenbach, M. Hans, D. Primetzhofer, J. M. Schneider and C. Scheu, *Nanoscale*, 2023, **15**, 17356–17363.
33 R. Sahu, D. Bogdanovski, J.-O. Achenbach, J. M. Schneider and C. Scheu, *Nanoscale*, 2022, **14**, 2578–2585.
34 R. Sahu, D. Bogdanovski, J. O. Achenbach, S. Y. Zhang, M. Hans, D. Primetzhofer, J. M. Schneider and C. Scheu, *Nanoscale*, 2021, **13**, 18077–18083.
35 K. H. J. Buschow, *J. Less-Common Met.*, 1965, **9**, 452–456.
36 S. Okada, K. Iizumi, K. Kudaka, K. Kudou, M. Miyamoto, Y. Yu and T. Lundström, *J. Solid State Chem.*, 1997, **133**, 36–43.
37 D. Bogdanovski, P. J. Pöllmann and J. M. Schneider, *Nanoscale*, 2022, **14**, 12866–12874.
38 Y. Zhou, H. Xiang, F.-Z. Dai and Z. Feng, *Mater. Res. Lett.*, 2017, **5**, 440–448.
39 I. A. Abrikosov, A. Knutsson, B. Alling, F. Tasnádi, H. Lind, L. Hultman and M. Odén, *Materials*, 2011, **4**, 1599–1618.
40 B. Martins, C. Patacas, A. Cavaleiro, P. Faia, O. Bondarchuk and F. Fernandes, *Surf. Coat. Technol.*, 2023, **464**, 129545.
41 L. J. V. D. Pauw, *Philips Tech. Rev.*, 1958, **20**, 220–224.
42 L. J. V. D. Pauw, *Philips Res. Rep.*, 1958, **13**, 1–9.
43 A. Huon, D. Lee, A. Herklotz, M. R. Fitzsimmons, H. N. Lee and S. J. May, *APL Mater.*, 2017, **5**(9), 096105.
44 A. Limaiem and F. Trochu, *Comput. Graph.*, 1995, **19**, 391–403.
45 A. Abdulkadhim, M. to Baben, V. Schnabel, M. Hans, N. Thieme, C. Polzer, P. Polcik and J. M. Schneider, *Thin Solid Films*, 2012, **520**, 1930–1933.
46 P. Ström and D. Primetzhofer, *J. Instrum.*, 2022, **17**, P04011.
47 P. Ström, P. Petersson, M. Rubel and G. Possnert, *Rev. Sci. Instrum.*, 2016, **87**, 103303.
48 Y. Zhang, H. J. Whitlow, T. Winzell, I. F. Bubb, T. Sajavaara, K. Arstila and J. Keinonen, *Nucl. Instrum. Methods Phys. Res., Sect. B*, 1999, **149**, 477–489.
49 M. Janson, *Internal Report*, Uppsala University, 2004.